Geophysical Research Letters

RESEARCH LETTER
10.1029/2022GL100468

Nanoscale Damage Production by Dynamic Tensile Rupture in α-Quartz

Marthe G. Guren[1], Henrik A. Sveinsson[1], Anders Malthe-Sørenssen[1], and François Renard[1,2]

[1]The Njord Centre, Departments of Geosciences and Physics, University of Oslo, Oslo, Norway, [2]ISTerre, University Grenoble Alpes, Grenoble INP, University Savoie Mont Blanc, CNRS, IRD, University Gustave Eiffel, Grenoble, France

Key Points:

- Molecular dynamics simulations of transient tensile stress produced by dynamic shear rupture show damage formation at the nanoscale
- A crack path instability occurs when tensile rupture speed is greater than 15% of the Rayleigh wave speed
- Crack microbranching leads to the production of nanoparticles and nano-roughness in a fault zone before frictional slip occurs

Supporting Information:

Supporting Information may be found in the online version of this article.

Correspondence to:

M. G. Guren,
m.g.guren@geo.uio.no

Citation:

Guren, M. G., Sveinsson, H. A., Malthe-Sørenssen, A., & Renard, F. (2022). Nanoscale damage production by dynamic tensile rupture in α-quartz. *Geophysical Research Letters*, *49*, e2022GL100468. https://doi.org/10.1029/2022GL100468

Received 25 JUL 2022
Accepted 4 OCT 2022

Abstract The creation of new fractures during an earthquake produces rock damage and contributes to the dissipation of strain energy. During dynamic rupture propagation, tensile microfractures can form in the earthquake process zone and in the domains around a fault that host large transient tensile stress. These microfractures can produce rock fragments with a wide range of sizes. Using molecular dynamics simulations, we model tensile rupture propagation in α-quartz under conditions of stress that occur during earthquake propagation. Our results show that for rupture speeds below 15% of the Rayleigh wave speed, fractures propagate linearly. At higher speeds, fracture propagation undergoes path instabilities with crack oscillations and microbranching leading to the formation of nanoscale roughness and fragments. This nanoscale damage can form in and around the earthquake process zone before any significant slip has occurred on the fault. The produced nanoparticles may control further energy dissipation during frictional slip.

Plain Language Summary During the propagation of earthquakes, the creation of new fractures produces damage at all scales in the fault zone and in the surrounding rock. However, the mechanisms of damage production at the nanoscale remain enigmatic. It is known that for brittle materials, crack propagation may evolve from planar to a pattern that includes oscillations above a threshold rupture speed. Here we show that, using α-quartz as a representative material for crystalline rocks, dynamic crack propagation involves oscillations and microbranching events during which two cracks propagate simultaneously until one branch dominates. The aborted branch and the propagating branch produce rock fragments with nanoscale dimensions that may control how energy is dissipated during earthquakes.

1. Introduction

Faulting of brittle rocks is preceded and controlled by tensile microfractures (e.g., Hadley, 1976; Katz & Reches, 2004; Reches & Lockner, 1994; Tapponnier & Brace, 1976). As the microfractures start interacting, a shear rupture may nucleate and propagate dynamically (Reches & Lockner, 1994). The dynamic propagation of microfractures before and during earthquakes produces damage along faults at all scales, including the formation of nanoparticles (e.g., Aretusini et al., 2017; Chester et al., 2005; Wilson et al., 2005). These nanoparticles can weaken the fault surface such that friction is reduced dramatically during seismic slip (Green II et al., 2015; Han et al., 2011; Hirose et al., 2012). Several mechanisms have been proposed to explain the formation of nanoparticles observed in fault zones, and involve grinding and sliding during slip at subseismic or seismic velocities (e.g., Aretusini et al., 2017; Keulen et al., 2007; Pec & Al Nasser, 2021; Verberne et al., 2014). Here, we propose another mechanism for nanoparticle formation in fault zones that is controlled by the dynamic propagation of tensile microfractures due to large transient tensile stresses produced in and around the earthquake rupture tip, before significant slip has occurred on the fault.

During earthquake rupture, the damage along the fault and in the surrounding rocks may lead to rock pulverization above a strain rate threshold (Doan & Gary, 2009). Pulverized rocks are characterized by multi-scale fractures (e.g., Dor et al., 2006; Rempe et al., 2013) and rock fragments with sizes ranging from sub-micrometers to centimeters, often having power-law size distributions (Keulen et al., 2007; Muto et al., 2015; Sammis et al., 1987). They can be found at a distance from the slip zone when formed by transient tensile stress perturbations (Griffith et al., 2018). Models of shear rupture propagation indicate that earthquake rupture activates both tensile and shear fractures (Okubo et al., 2019) and these fractures create off-fault damage patterns that are consistent with field observations (Thomas & Bhat, 2018). The observation of asymmetric damage zones in faults may occur due to the propagation of ruptures along a bi-material interface, producing high tensile stresses on one

side of the rupture (e.g., Andrews, 2005; Ben-Zion & Shi, 2005; Di Toro and Pennacchioni, 2005; Petley-Ragan et al., 2019; Reches & Dewers, 2005). On the side of the fault that experiences high tensile stress, tensile microfractures may propagate, a process that splits the rock into fragments (Katz & Reches, 2004; Rice et al., 2005; Tapponnier & Brace, 1976).

A tensile microfracture may develop as a planar crack that propagates in a stable manner along a single fracture plane (e.g., Bouchbinder et al., 2014), or it may become unstable when the crack tip oscillates during propagation in the direction of the maximum stress, which may lead to microbranching (e.g., Bleyer & Molinari, 2017). The type of propagation varies with rupture speed. At low speeds, fracture surface roughness may develop with three morphologies: mirror, mist, and hackle (Buehler, 2008; Fineberg et al., 1991). For mirrors, the crack propagates at low speeds creating a perfect cleavage, and as the speed increases, the crack surface changes from slightly rough (mist) to significantly rough (hackle). The mirror-mist-hackle regimes have been observed in experiments (e.g., Fineberg et al., 1991), as well as in models containing a perfect atomic lattice (e.g., Abraham et al., 1997; Buehler & Gao, 2006). Dynamic instabilities at the crack tip decrease the rupture propagation speeds below C_R, the Rayleigh wave speed predicted for dynamic planar cracks by linear elastic fracture mechanics (Fineberg et al., 1991). The transition between the stable and unstable propagation regimes occurs when the crack tip speed exceeds a critical value that has been measured experimentally in several materials: $0.44C_R$ for silica glass and polymethyl methacrylate (Fineberg et al., 1991; Sharon and Fineberg, 1996, 1998), and $0.34C_R$ for neo-Hookean brittle gels (Livne et al., 2005). Above these critical rupture speeds, the crack tip propagation deviates from linear to oscillations or branch into two or more cracks. Crack instabilities have been observed all the way down to the nanoscale (e.g., Buehler & Gao, 2006; Zhou et al., 1996), where dynamic tensile fractures nucleate when the breaking of an interatomic bond starts an avalanche of subsequent bond breakage, resulting in the propagation of a crack across length scales.

Here, we simulate dynamic tensile fracture and damage generation at the molecular level in a single α-quartz grain. We simulate different crystallographic orientations of the quartz grain to account for the multi-grain nature of a fault zone. We aim to quantify under which conditions microfractures with nanoscale roughness and nanoparticles may form near the rupture tip, in the earthquake process zone or in the tensile domain of the fault zone before significant slip has occurred on the fault surface. We infer that the nano-roughness of microfractures and the nanoparticles produced dynamically may control the shear strength and damage production in the fault zone during seismic slip.

2. Methods

2.1. Simulation Setup and Procedure

The setup consists of a three-dimensional block of α-quartz with a pre-cracked notch structure (Figure 1a). The block is cut along three crystallographic planes, and the orientation of the system (Figure 1b) is such that the *xy* plane (*z*-cut) corresponds to the (0 0 0 1) crystallographic plane, the *yz* plane (*x*-cut) is the $(\bar{2}\,1\,1\,0)$ crystallographic plane and the *xz* plane (*y*-cut) is the $(0\,\bar{1}\,1\,0)$ crystallographic plane. The system is periodic in the *y*-direction, while the boundaries at top, bottom and both ends in the *x*-direction are fixed in order to apply a specific stress state.

First, a compressive normal stress is imposed along the *x*-direction using an isothermal-isobaric thermostat since rocks at depth experience a compressive stress regime. Then, an extensional displacement controlled by the canonical ensemble is imposed along the *z*-direction, perpendicularly to the notch. The imposed tensile loading leads to an initial tensile stress in the range 1,000–2,000 MPa, measured just before the crack starts propagating. These levels of tensile stress agree with expectations for earthquake propagation in the crust where GPa-level transient tensile stresses are simulated near a shear rupture tip (e.g., Figure 5 in Reches & Dewers, 2005). For most simulations, the imposed compressive stress in the *x*-direction is 500 MPa, the extensional displacement along the *z*-axis is imposed over a period of 3×10^{-11} s, and the temperature is set to 300 K, such that the simulations are at a safe distance from the α-ß transition of quartz, which for the model occurs at around 700 K (Karlsen, 2022).

The simulations are run for 5×10^{-10} s with a time step of 1×10^{-15} s, during which a tensile (mode I) dynamic crack propagates. Depending on the initial tensile stress imposed on the system, one of three outcomes are observed: (a) the crack does not propagate from the initial notch; (b) the crack starts propagating and stops inside

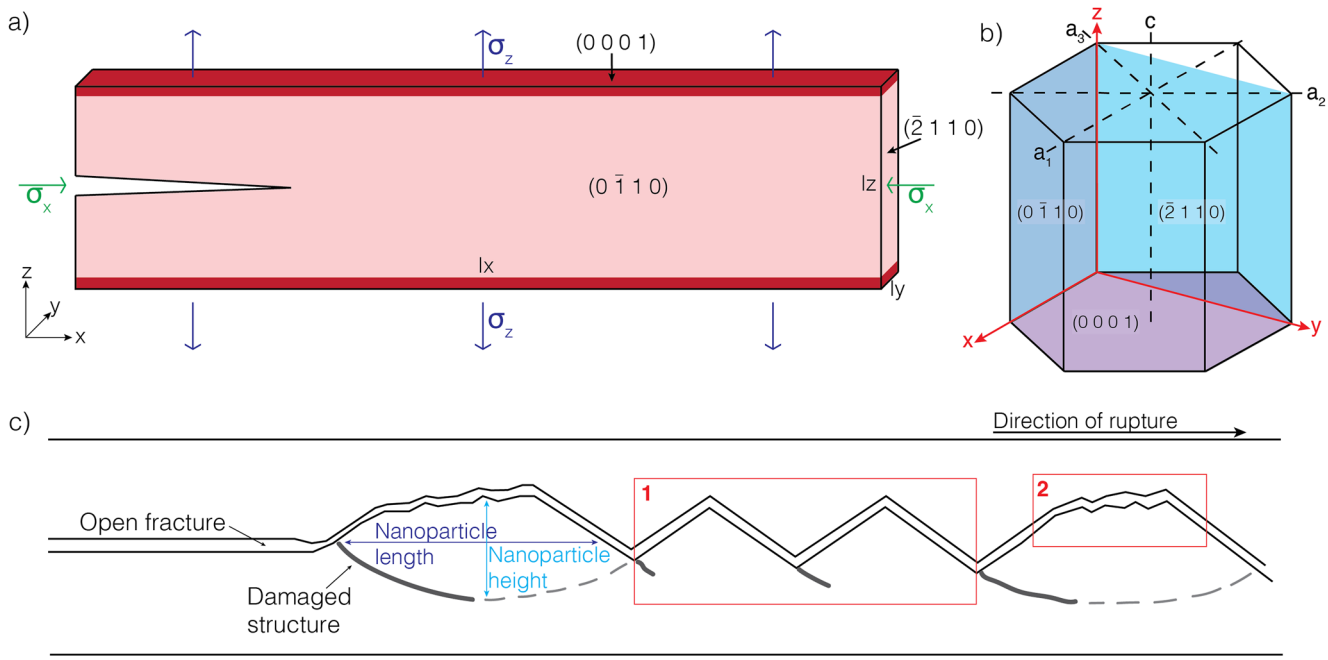

Figure 1. (a) Sketch of the simulation setup of a three-dimensional block of α-quartz that contains 1.63×10^7 atoms ($l_x = 300$ nm, $l_y = 12$ nm, $l_z = 60$ nm). The length of the initial notch that guides tensile fracture propagation is 60 nm, and the aperture is 1.6 nm on the left side. The upper and lower parts of the block (red areas) are fixed. The block is exposed to a compressive normal stress along the x-direction (σ_x), followed by a tensile strain along the z-direction (σ_z). (b) Orientation of the block with a x-, y-, and z-cut in α-quartz. Both the crystallographic axes (a_1, a_2, a_3 and (c) and the coordinates axes (x, y, and z) used in our simulations are shown. (c) A sketch of a fracture, drawn from a simulation snapshot, show the formation of nanoscale fragments and nanoscale fracture roughness. Solid lines represent observed damage while the dashed line represent potential damage at the atomic scale. Box 1 (red) illustrates a propagation path influenced by the crystallographic structure (see Figure 2d), whereas box 2 (red) illustrates an area where the propagation path is less influenced by the crystallographic structure (see Figure 2e).

the simulation domain; or (c) the crack propagates throughout the simulation domain along the x-direction. If the crack does not propagate, the simulation is discarded because the loading was insufficient for dynamic crack propagation. If the crack propagates, but does not cross the whole domain, we increase the duration of the simulation such that the crack reaches the end of the simulation domain. Thus, we obtain a set of simulations where a crack has propagated throughout the entire system. We sample the position of the crack tip in the x-direction through time and calculate the average rupture speed. To assess the sensitivity of the rupture speed on the details of the simulation setup, we varied the loading plane, compressive stress, temperature, and loading rate. The effect of these variables on the rupture speed is described (Table S4 and Figures S5–S8 in Supporting Information S1), but overall the rupture speed is not particularly sensitive to these parameters and we observe the same qualitative behavior.

2.2. Interatomic Interaction Potential for α-quartz

We perform the simulations using the molecular dynamics package LAMMPS (Plimpton, 1995), using the Vashishta potential. The 1997-version of the potential (Broughton et al., 1997) is optimized toward the material properties of crystalline α-quartz and it is a modified version of the Nakano et al. (1994) three-body potential, which was modified from the original version of the potential (Vashishta et al., 1990). Tables S1 and S2 in Supporting Information S1 display the parameters used in the simulations. To ensure that the simulated material has properties similar to α-quartz within the pressure and temperature range of our simulations, we have calculated the elastic parameters, density, and the compressibility parameters of the lattice along different crystalline directions (see Figures S2–S4 in Supporting Information S1) and found that it is in agreement with experimental measurements (e.g., Jorgensen, 1978; d'Amour et al., 1979; Hazen et al., 1989; Glinnemann et al., 1992). Based on the elastic parameters (Table S3 in Supporting Information S1) and the density, the Rayleigh wave speed is 3,048 m/s when applying an extensional displacement on the (0 0 0 1) plane and 3,097 m/s when applying an extensional displacement on the (0 $\bar{1}$ 1 0) plane, using the procedure of Vinh and Ogden (2005).

3. Results

For all the simulations, we describe the fracture surface roughness after the crack has propagated through the simulation domain by classifying the fracture geometry as planar cracks, wavy cracks created by an oscillating rupture tip, and cracks exhibiting microbranching (Figure 2). When the crack tip oscillates, we measure the amplitude of the produced roughness (Figure 2f). For the planar cracks (Figure 2a), the propagation produces a combination of mirror and mist surface roughness. In some areas, the crack propagates along a single atomic plane, producing a mirror surface (Figure 2a, box 1). In other areas, the crack propagation creates a mist surface, by shifting between atomic layers (Figure 2a, box 2). Wherever the crack changes course or turns abruptly (Figure 2d), or where the crack branches (Figure 2e), atomic scale damage is created in the surrounding quartz structure. This damage is characterized by a lower atomic density, and corresponds to disorder at the atomic scale.

We measure the rupture speed in every simulation by sampling the position of the crack tip in the x-direction through time and identify the critical speed for crack tip oscillations and branching. Figure 3a shows how rupture speed and crack path vary with the initial tensile stress imposed on the system. Based on observations of features (Figures 2a–2e), a qualitative difference is observed between Figures 2b and 2c. In Figure 2b, the crack propagates mostly planar but jump between atomic layers, while in Figure 2c, it never has a planar propagation. This change in propagation behavior is observed when the initial tensile stress is around 1,210 MPa and the rupture speed remains below 460 m/s, equivalent to $0.15C_R$ (Figure 3a). When the initial tensile stress increases, the rupture speed increases as well, and the crack tip propagation oscillates (Figures 2c and 2d). For initial tensile stresses larger than 1,600 MPa, crack microbranching occurs, and the rupture speed exceeds 800 m/s, corresponding to $0.26C_R$ (Figure 3a). During a branching event, two cracks propagate simultaneously until one of the cracks dominates, from which the dynamic rupture propagation continues (Figure 2e). In Figure 3a, we observe that the slope of rupture speed versus initial tensile stress is steepest before the crack tip start oscillating. However, when approaching an initial tensile stress where the crack tip oscillates, the rupture speed stagnates before it continues to increase, indicating that there is an energy barrier to overcome. Similarly, a stagnation of the curve is observed around the threshold speed where microbranches start developing.

The perfect quartz lattice is an energy minimum for our system. One way to characterize the damage caused by crack propagation is to compare the potential energy of the relaxed initial system with the potential energy of the relaxed state after the crack has propagated through the system (Figure S9 in Supporting Information S1). To obtain high crack speeds, the system has to be loaded substantially above the fracture toughness (overstress) of the material, and the amount of overstress controls the rupture speed and dissipated energy (Svetlizky et al., 2017). Therefore, the available strain energy is much larger than the energy needed to open the crack surface, leading to thermal energy being released during crack propagation. The released thermal energy is absorbed by the thermostat during and after crack propagation and we make sure to measure the potential energy at the same temperature for the initial state and the cracked state. The potential energy is averaged over the last 5×10^{-11} s of each simulation, and this averaging window starts at least 5×10^{-12} s after the crack has reached the far end of the sample. For a perfectly planar crack, this energy difference should be equal to $2A\gamma_{s,}$ where γ_s is the surface energy of a flat crack surface and A is the surface area of the new crack (A. A. Griffith, 1920). In our simulations, the surface energy for planar cracks was found to be equal to 0.93 J/m^2. For comparison, the surface energy of the (0 0 0 1) plane of quartz in air has been measured experimentally to be 0.92 J/m^2 (Parks, 1984). Figure 3b shows how the dissipated energy varies with rupture speed. The results show that the energy dissipated in the system increases with increasing rupture speed due to crack tip oscillation and microbranching that damages the material. The contribution of potential energy of new surfaces and damaged quartz structures varies for the oxygen and silicon atoms (Figures S10a and S11a in Supporting Information S1). For the silicon atoms, the new surfaces provide a higher potential energy than the damaged structures. Conversely, for the oxygen atoms, the energy in the new surfaces is lower than in the damaged structure. This can be explained by the energy from the steric repulsion and the Coulomb interactions between oxygen pairs (see Supporting Information S1).

4. Discussion

4.1. Morphology of Fractures

Fracture surfaces have been studied extensively in model brittle materials, such as polymethyl methacrylate (e.g., Fineberg et al., 1991; Sharon & Fineberg, 1996), Homalite (Ravi-Chandar & Knauss, 1984), silica glass (Sharon

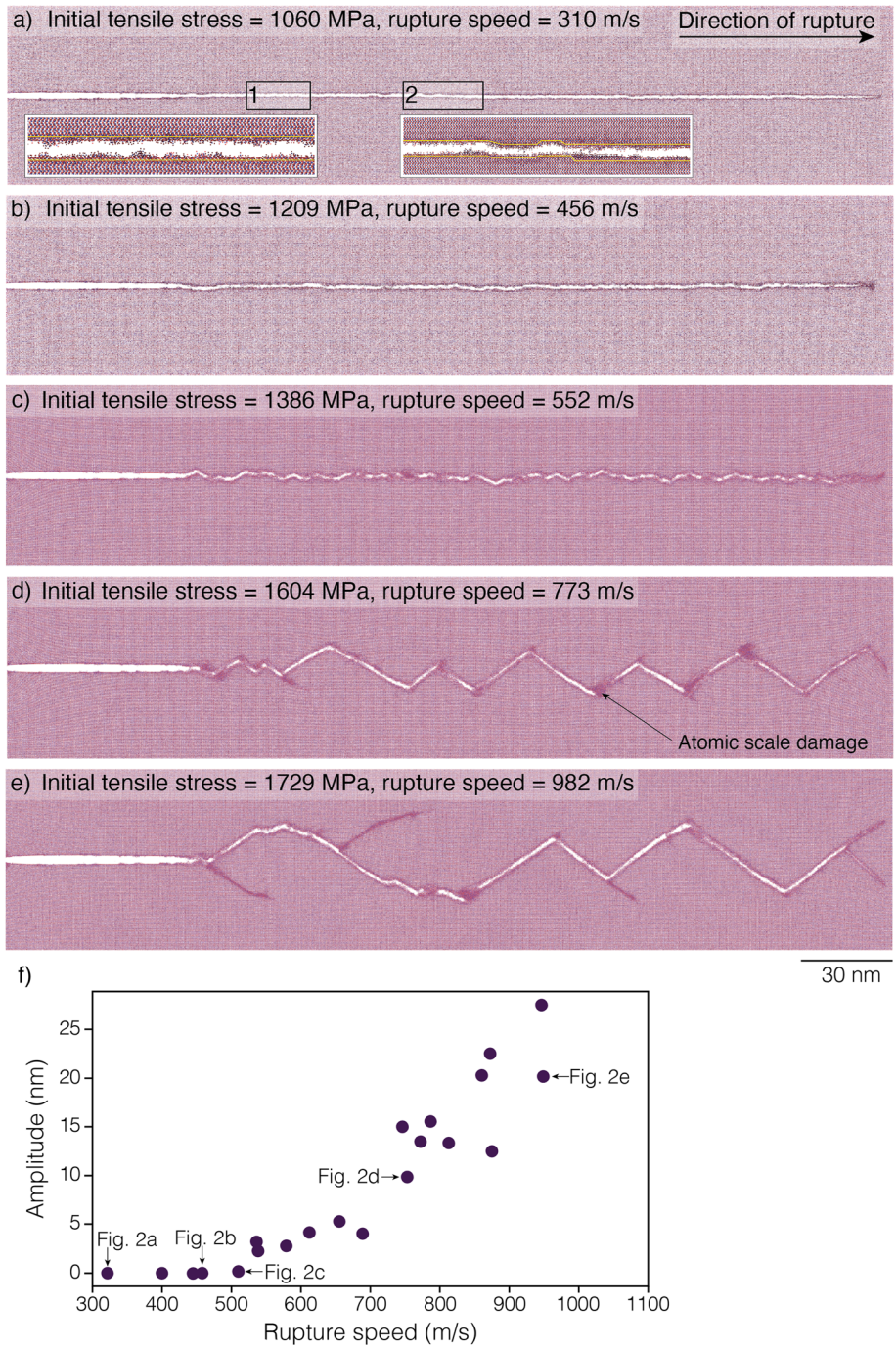

Figure 2. Snapshots of the atoms in the simulation system with a fracture (white) and damage (dark red) after the crack has propagated through α-quartz. The darker red colored areas (black arrow) and areas with microbranching correspond to damage in the quartz structure by breakage of the atomic bonds. (a) Initial tensile stress of 1,060 MPa, the crack propagates along an atomic plane. Area 1 shows a mirror surface, while area 2 shows mist. The yellow lines in the inset figures indicate the atomic layer along which the fracture propagates. (b) Initial tensile stress of 1,209 MPa, the crack propagates mostly planar. (c) Initial tensile stress of 1,386 MPa, the crack tip propagation oscillates out-of-plane (hackle pattern). (d) Initial tensile stress of 1,604 MPa, the crack tip oscillations induce a more pronounced wavy surface. (e) Initial tensile stress of 1,729 MPa, crack branching occurs. (f) Amplitude of the produced roughness as a function of rupture speed.

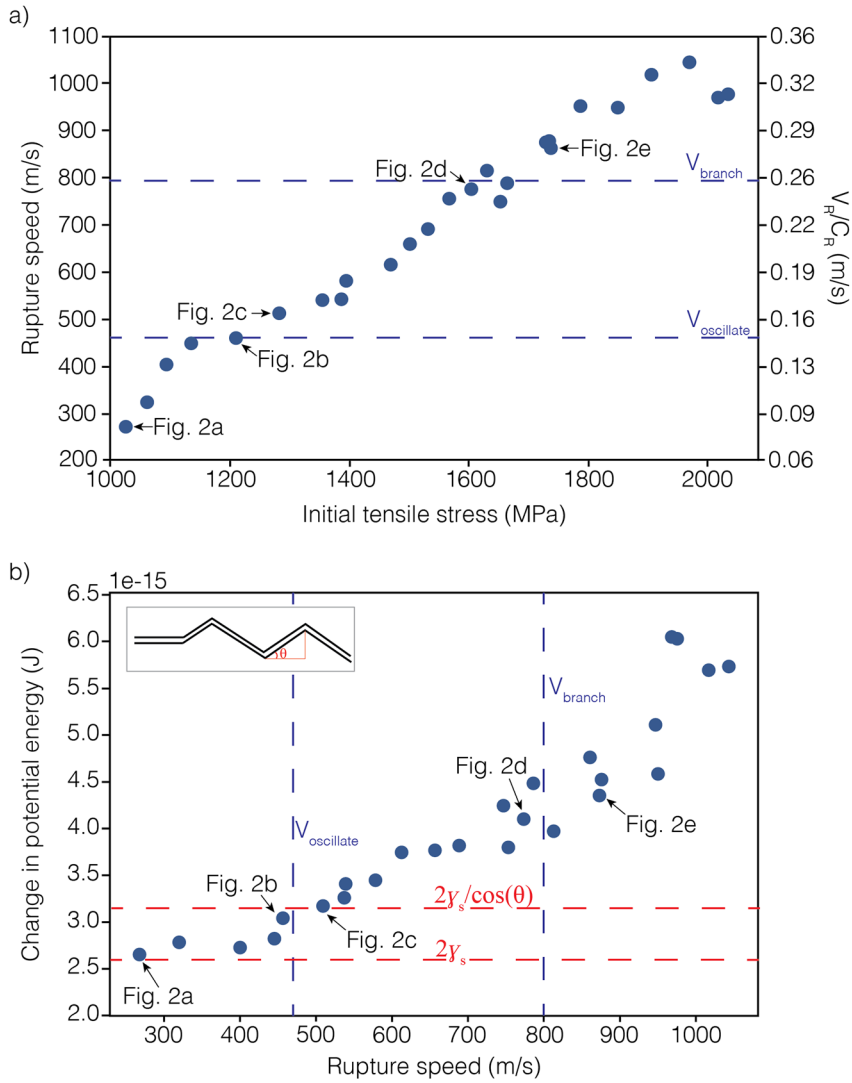

Figure 3. (a) Rupture speed (V_R) of the crack tip as a function of initial tensile stress. Above a critical speed $V_{oscillate} = 0.15C_R$, where C_R is the Rayleigh wave speed, the crack tip oscillates. Above a critical speed $V_{branch} = 0.26C_R$, crack branching occurs. (b) Change in potential energy of the simulation domain from the relaxed initial system and the relaxed state after the crack has propagated through the domain, as a function of rupture speed. γ_s is the surface energy and θ is the angle of the crack.

& Fineberg, 1998) or neo-Hookean brittle gels (Livne et al., 2005). These studies showed that, above a threshold rupture speed, the crack surface changed from smooth to a jagged structure that undergoes instabilities characterized by either wavy roughness or microbranching. Our results show a similar trend, where the morphology of a crack surface in a model α-quartz varies with rupture speed. At low speeds, the crack is propagating planar (Figure 2a). When the rupture speed increases, the crack undergoes path instabilities first by oscillations of the crack tip, where the amplitude of the produced roughness increases as the crack speed increases (Figures 2c, 2d and 2f) and then, at higher rupture speeds by branching (Figure 2e).

Because polymethyl methacrylate is an amorphous material, Fineberg et al. (1991) and Sharon and Fineberg (1996) argued that the source of the observed wavy structures in the experiments could not be linked to the material structure. Instead, the occurrence of the crack tip oscillations was attributed to a sudden increase in rupture speed. In contrast to an amorphous material, we observe that fracture propagation is controlled by the crystalline structure of α-quartz to some degree. For example, the atom layers control the transition from mirror to mist surface as the crack jumps between different layers. At the onset of crack tip oscillations, the produced roughness has a small

amplitude, is irregular and does not seem to follow the crystalline structure (e.g., Figure 2c). However, when the wavy roughness reaches a more regular amplitude, it follows the crystalline structure of quartz (e.g., Figures 1c and 2d). During microbranching, certain areas with the wavy structure are controlled by the crystalline structure while, in other areas, zones of damage show a slightly rounded shape (Figure 1c), which cannot be directly linked to the crystalline structure of α-quartz.

4.2. Rupture Velocity and Crack Instabilities

The threshold rupture speed above which path instabilities are observed has been measured in several materials and found to be in the range 0.3–0.74C_R (e.g., Bleyer & Molinari, 2017; Buehler & Gao, 2006; Zhou et al., 1996), and experiments on single-crystal quartz observed branching when the crack approached 0.45C_R (Leong et al., 2018). The first Molecular dynamics simulations of 2D homogenous brittle solids with linear elastic properties found that crack branching occur at a rupture speed of 0.35C_R (Zhou et al., 1996), while a later study indicated a threshold of 0.73C_R (Buehler & Gao, 2006). In our simulations, we have identified two threshold speeds: $V_{oscillate} = 0.15C_R$ is the speed of the first path instability that produces a wavy surface due to the crack tip oscillations around the direction of the main compressive stress, and nanoroughness, and $V_{branch} = 0.26C_R$ is the speed at which the first microbranching is observed. These two speeds are slightly lower than experimental measurements performed in quartz on larger samples and significantly lower than the theoretical limit of C_R. However, such slow speeds have also been observed in experiments on Berea Sandstone and Westerly Granite with speeds of 0.21C_R and 0.12C_R, respectively (Braunagel & Griffith, 2022). In the next paragraph, we propose that the difference in crack speeds in our simulations and measured experimentally in single quartz crystals is due to the functional form of the cohesive force between silicon and oxygen atoms.

Buehler and Gao (2006) modeled an elastic 2D material and tuned the cohesive force between interacting atoms to study how this parameter controls rupture speed. The cohesive force is dependent on the breaking of atomic bonds, which occurs at a critical atom separation (r_{break}). This critical atom separation can be expressed as the ratio between the interatomic distance where the potential energy slope is steepest, and the minimum potential energy. It is one of the key parameters governing the crack instability speed. When $r_{break} = 1.135$, a dynamic instability can occur for rupture velocities below 0.2C_R, whereas when r_{break} increases to 1.25, a dynamic instability occurs for rupture velocities above 0.73C_R. In the interatomic potential used in our simulations, r_{break} for the two-body interactions between silicon and oxygen atoms is equal to 1.144 (Figure S1 in Supporting Information S1). This value falls in the lower range of investigated r_{break} parameters (Buehler & Gao, 2006) and is consistent with the threshold speeds for crack propagation instabilities in the range 0.15–0.32C_R observed in our simulations. It is therefore likely that the shape of the two-body interaction between silicon and oxygen, and in particular the critical separation r_{break} governs the rupture speed. In future adjustments of the parameters of silica potentials, one should therefore consider this quantity explicitly.

4.3. Production of Nanoscale Damage During Dynamic Rupture Propagation

Damage zones in faults contain a high density of fractures at all scales, which may be created by several processes occurring before, during and after the fault formation, such as Andersonian fracturing, early fault tip migration, fault tip linkage (e.g., Johri et al., 2014; Mitchell & Faulkner, 2009), thermal cracking by heat diffusion (Passelègue et al., 2016), rock pulverization (Dor et al., 2006), and dynamic ruptures (Paul et al., 2007; Rudnicki, 1980; Wilson et al., 2003). Models of dynamic rupture calculate the stress field around a fault tip during propagation, which allows quantifying the damage along the length of the rupture (e.g., Andrews, 1976; Madariaga, 1976) and tensile stress are produced in the rupture process zone and near the fault (e.g., Okubo et al., 2019). Our simulations indicate that a propagating tensile crack creates nanoscale damage in the form of nano-roughness and nanoparticles. This damage is generated in the material surrounding the propagating tensile crack and aborted branches (e.g., Figure 2d). The damage produced in our simulations is reminiscent of what happens during the formation of pulverized rocks, which have been shattered in situ without significant shear strain, and consists of very fine grains (e.g., Dor et al., 2006). Dynamic pulverization produces both intragranular and intergranular fractures (e.g., Doan & Gary, 2009; Dor et al., 2006). Our simulations represent intergranular fractures in single grains with various crystallographic orientations to account for the multi-grain nature of a fault zone when multiple tensile microfractures propagate through the grains.

If our damaged crystals were exposed to further strain through shear deformation, this would lead to the formation of more nanosized fragments, by the wear of nano-roughness (Figure 1c). For nanoparticles formed during slip, previous work has suggested that some materials have a minimum fragment size achieved through grinding, that is, the grinding limit (Kendall, 1978). For quartz, the grinding limit is 0.9 μm (Prasher, 1987); however, quartz grains with radius of 15 nm have been observed in both experiments and naturally produced gouges (Keulen et al., 2007). The observations of rock fragments with dimensions below the grinding limit prompts a reexamination of the mechanical origin of these fragments.

In our simulations where rupture propagation produces microbranches, we have measured the height and length of nascent fragments. Independently of the initial tensile stress and the height of the system (Figure S12 in Supporting Information S1), the height of the fragments would be around 20 nm, while their length would vary in the range 40–110 nm. For cracked grains in a gouge, the lower limit for fragment diameter is reported to be 30 nm; however, the fragments can also reach sizes up to 100 μm (Keulen et al., 2007). For grain sizes below 1.2 ± 0.3 μm, Keulen et al. (2007), who studied fragmentation formed under confining pressure, proposed that these grains are produced by another mechanism than grinding. Sammis and Ben-Zion (2008) explored mechanisms that might produce fragment below the grinding limit and showed that nanometer-sized fragments rarely form by grain crushing in simple shear under compressive loading but could be produced during tensile loading at high strain rates. An estimate of the smallest fragment produced by tensile stress can be found by $\boldsymbol{K_{IC} = \sigma\sqrt{\pi a}}$, where K_{IC} is the fracture toughness and 1 MPa $m^{1/2}$ for quartz (e.g., Iwasaki & Torikai, 1993), $\boldsymbol{\sigma}$ is the tensile stress and a is the radius of the flaw. In our simulation, the tensile stress is in the range 1–2 GPa, which will give a = 80–320 nm. If the flaws are almost equal in size and distributed uniformly in the rock, a will indicate the dimensions of the fragments, otherwise even smaller fragments could be formed (Sammis & Ben-Zion, 2008). From our simulations, even the longest fragments (110 nm) are much smaller than the grinding limit for quartz and in the lower range of estimated fragment sizes due to tensile loading condition. Therefore, dynamic rupture at molecular scale could provide an explanation for the formation of rock fragments with dimensions smaller than the grinding limit. This is supported by Wilson et al. (2005) who argued that the smallest fragments in gouges might be explained by damage emanating from a crack tip during dynamic rupture.

5. Conclusion

We perform molecular scale simulations of dynamic rupture propagation in α-quartz loaded under tensile stress and show the production of nanoscale fracture roughness and nanoparticles. Our result on quartz may be extended to other minerals such as carbonates, for which nanoparticles have been observed in experimental faults (Siman-Tov et al., 2015). We identify critical tensile rupture speeds for crack tip oscillations and crack branching that are consistent with results from Buehler and Gao (2006). When the rupture speed is below 460 m/s ($0.15C_R$), the crack tip propagates planar, while at higher speeds it starts oscillating, producing nanoscale fracture roughness. For rupture speeds above 800 m/s ($0.26C_R$), microbranching occur, an event where two branches propagate simultaneously until one branch dominates. These two branches may provide an initial structure that could lead to nanosized fragments with dimensions below the grinding limit. The nanoscale damage studied here occurs near the tip of a propagating earthquake, before significant slip (or shear strain) has occurred on the faults plane. The nanoscale particles and nanoscale roughness produced at the rupture tip may then contribute to modify the frictional strength of the fault during seismic slip.

Data Availability Statement

All research data and numerical codes necessary to reproduce the results of the study are available from Zenodo at https://doi.org/10.5281/zenodo.5873712 (Guren, 2022).

Acknowledgments
We thank Fabian Barras and Jessica McBeck for useful and constructive suggestions on an early version of the manuscript. This work was funded by the Research Council of Norway (project History Dependent Friction 287084 to AMS) and the European Research Council (ERC) under the European Union's Horizon 2020 research and innovation program (Grant 101019628 BREAK to FR).

References

Abraham, F. F., Brodbeck, D., Rudge, W. E., & Xu, X. (1997). A molecular dynamics investigation of rapid fracture mechanics. *Journal of the Mechanics and Physics of Solids*, *45*(9), 1595–1619. https://doi.org/10.1016/s0022-5096(96)00103-2

Andrews, D. J. (1976). Rupture propagation with finite stress in antiplane strain. *Journal of Geophysical Research*, *81*(20), 3575–3582. https://doi.org/10.1029/jb081i020p03575

Andrews, D. J. (2005). Rupture dynamics with energy loss outside the slip zone. *Journal of Geophysical Research*, *110*(1), 1–14. https://doi.org/10.1029/2004jb003191

Aretusini, S., Mittemperher, S., Plümper, O., Spagnuolo, E., Gualtieri, A. F., & Di Toro, G. (2017). Production of nanoparticles during experimental deformation of smectite and implications for seismic slip. *Earth and Planetary Science Letters*, *463*, 221–231. https://doi.org/10.1016/j.epsl.2017.01.048

Ben-Zion, Y., & Shi, Z. (2005). Dynamic rupture on a material interface with spontaneous generation of plastic strain in the bulk. *Earth and Planetary Science Letters*, *236*(1–2), 486–496. https://doi.org/10.1016/j.epsl.2005.03.025

Bleyer, J., & Molinari, J. F. (2017). Microbranching instability in phase-field modelling of dynamic brittle fracture. *Applied Physics Letters*, *110*(15), 151903. https://doi.org/10.1063/1.4980064

Bouchbinder, E., Goldman, T., & Fineberg, J. (2014). The dynamics of rapid fracture: Instabilities, nonlinearities and length scales. *Reports on Progress in Physics*, *77*(4), 046501. https://doi.org/10.1088/0034-4885/77/4/046501

Braunagel, M. J., & Griffith, W. A. (2022). Microstructural controls on mixed mode dynamic fracture propagation in crystalline and porous granular rocks. *Journal of Geophysical Research: Solid Earth*, *127*(3), e2021JB022528. https://doi.org/10.1029/2021jb022528

Broughton, J. Q., Meli, C. A., Vashishta, P., & Kalia, R. K. (1997). Direct atomistic simulation of quartz crystal oscillators: Bulk properties and nanoscale devices. *Physical Review B: Condensed Matter and Materials Physics*, *56*(2), 611–618. https://doi.org/10.1103/physrevb.56.611

Buehler, M. J. (2008). Atomistic modeling of materials failure, Springer Science & Business Media.

Buehler, M. J., & Gao, H. (2006). Dynamical fracture instabilities due to local hyperelasticity at crack tips. *Nature*, *439*(7074), 307–310. https://doi.org/10.1038/nature04408

Chester, J. S., Chester, F. M., & Kronenberg, A. K. (2005). Fracture surface energy of the Punchbowl fault, San Andreas system. *Nature*, *437*(7055), 133–136. https://doi.org/10.1038/nature03942

d'Amour, H., Denner, W., & Schulz, H. (1979). Structure determination of α-quartz up to 68 x 108 Pa. *Acta Crystallographica Section B: Structural Crystallography and Crystal Chemistry*, *35*(3), 550–555.

Di Toro, G., & Pennacchioni, G. (2005). Fault plane processes and mesoscopic structure of a strong-type seismogenic fault in tonalites (Adamello batholith, Southern Alps). *Tectonophysics*, *402*(1–4), 55–80. https://doi.org/10.1016/j.tecto.2004.12.036

Doan, M. L., & Gary, G. (2009). Rock pulverization at high strain rate near the San Andreas fault. *Nature Geoscience*, *2*(10), 709–712. https://doi.org/10.1038/ngeo640

Dor, O., Ben-Zion, Y., Rockwell, T. K., & Brune, J. (2006). Pulverized rocks in the Mojave section of the San Andreas fault zone. *Earth and Planetary Science Letters*, *245*(3–4), 642–654. https://doi.org/10.1016/j.epsl.2006.03.034

Fineberg, J., Gross, S. P., Marder, M., & Swinney, H. L. (1991). Instability in dynamic fracture. *Physical Review Letters*, *67*(4), 457–460. https://doi.org/10.1103/physrevlett.67.457

Glinnemann, J., King, H. E., Jr., Schulz, H., Hahn, T., La Placa, S. J., & Dacol, F. (1992). Crystal structures of the low-temperature quartz-type phases of SiO_2 and GeO_2 at elevated pressure. *Zeitschrift für Kristallographie—Crystalline Materials*, *198*(1–4), 177–212. https://doi.org/10.1524/zkri.1992.198.3-4.177

Green, H. W., II, Shi, F., Bozhilov, K., Xia, G., & Reches, Z. (2015). Phase transformation and nanometric flow cause extreme weakening during fault slip. *Nature Geoscience*, *8*(6), 484–489. https://doi.org/10.1038/ngeo2436

Griffith, A. A. (1920). The phenomena of rupture and flow in solids. *Philosophical Transactions of the Royal Society of London—Series A: Containing Papers of a Mathematical or Physical Character*, *221*(582–592), 163–198.

Griffith, W. A., Julien, R. C., St, Ghaffari, H. O., & Barber, T. J. (2018). A tensile origin for fault rock pulverization. *Journal of Geophysical Research: Solid Earth*, *123*(8), 7055–7073. https://doi.org/10.1029/2018jb015786

Guren, M. G. (2022). Supplementary data for "Nanoscale modelling of dynamic rupture and damage generation in alpha-quartz" [Dataset]. Zenodo. Retrived from https://doi.org/10.5281/zenodo.5873712

Hadley, K. (1976). Comparison of calculated and observed crack densities and seismic velocities in westerly granite. *Journal of Geophysical Research*, *81*(20), 3484–3494. https://doi.org/10.1029/jb081i020p03484

Han, R., Hirose, T., Shimamoto, T., Lee, Y., & Ando, J.-I. (2011). Granular nanoparticles lubricate faults during seismic slip. *Geology*, *39*(6), 599–602. https://doi.org/10.1130/g31842.1

Hazen, R. M., Finger, L. W., Hemley, R. J., & Mao, H. K. (1989). High-pressure crystal chemistry and amorphization of α-quartz. *Solid State Communications*, *72*(5), 507–511. https://doi.org/10.1016/0038-1098(89)90607-8

Hirose, T., Mizoguchi, K., & Shimamoto, T. (2012). Wear processes in rocks at slow to high slip rates. *Journal of Structural Geology*, *38*, 102–116. https://doi.org/10.1016/j.jsg.2011.12.007

Iwasaki, H., & Torikai, D. (1993). Thermal shock of quartz lascas. *Journal of Materials Science*, *28*(19), 5223–5228. https://doi.org/10.1007/bf00570068

Johri, M., Dunham, E. M., Zoback, M. D., & Fang, Z. (2014). Predicting fault damage zones by modeling dynamic rupture propagation and comparison with field observations. *Journal of Geophysical Research: Solid Earth*, *119*(2), 1251–1272. https://doi.org/10.1002/2013jb010335

Jorgensen, J. D. (1978). Compression mechanisms in α-quartz structures—SiO_2 and GeO_2. *Journal of Applied Physics*, *49*(11), 5473–5478. https://doi.org/10.1063/1.324517

Karlsen, N. (2022). *Evaluating the behavior of silica modeled by the Vashishta potential using free energy methods*. M.Sc. thesis, University of Oslo.

Katz, O., & Reches, Z. (2004). Microfracturing, damage, and failure of brittle granites: Microfracturing and failure of granites. *Journal of Geophysical Research*, *109*(B1), B01206. https://doi.org/10.1029/2002jb001961

Kendall, K. (1978). The impossibility of comminuting small particles by compression. *Nature*, *272*(5655), 710–711. https://doi.org/10.1038/272710a0

Keulen, N., Heilbronner, R., Stünitz, H., Boullier, A. M., & Ito, H. (2007). Grain size distributions of fault rocks: A comparison between experimentally and naturally deformed granitoids. *Journal of Structural Geology*, *29*(8), 1282–1300. https://doi.org/10.1016/j.jsg.2007.04.003

Leong, A. F. T., Robinson, A. K., Fezzaa, K., Sun, T., Sinclair, N., Casem, D. T., et al. (2018). Quantitative in situ studies of dynamic fracture in brittle solids using dynamic X-ray phase contrast imaging. *Experimental Mechanics*, *58*(9), 1423–1437. https://doi.org/10.1007/s11340-018-0414-3

Livne, A., Cohen, G., & Fineberg, J. (2005). Universality and hysteretic dynamics in rapid fracture. *Physical Review Letters*, *94*(22), 224301. https://doi.org/10.1103/physrevlett.94.224301

Madariaga, B. Y. R. (1976). Dynamics of an expanding circular fault. *Bulletin of the Seismological Society of America*, *66*(3), 639–666. https://doi.org/10.1785/bssa0660030639

Mitchell, T. M., & Faulkner, D. R. (2009). The nature and origin of off-fault damage surrounding strike-slip fault zones with a wide range of displacements: A field study from the Atacama fault system, northern Chile. *Journal of Structural Geology*, *31*(8), 802–816. https://doi.org/10.1016/j.jsg.2009.05.002

Muto, J., Nakatani, T., Nishikawa, O., & Nagahama, H. (2015). Fractal particle size distribution of pulverized fault rocks as a function of distance from the fault core. *Geophysical Research Letters*, *42*(10), 3811–3819. https://doi.org/10.1002/2015gl064026

Nakano, A., Kalia, R. K., & Vashishta, P. (1994). First sharp diffraction peak and intermediate-range order in amorphous silica: Finite-size effects in molecular dynamics simulations. *Journal of Non-Crystalline Solids*, *171*(2), 157–163. https://doi.org/10.1016/0022-3093(94)90351-4

Okubo, K., Bhat, H. S., Rougier, E., Marty, S., Schubnel, A., Lei, Z., et al. (2019). Dynamics, radiation, and overall energy budget of earthquake rupture with coseismic off-fault damage. *Journal of Geophysical Research: Solid Earth*, *124*(11), 11771–11801. https://doi.org/10.1029/2019jb017304

Parks, G. A. (1984). Surface and interfacial free energies of quartz. *Journal of Geophysical Research*, *89*(B6), 3997–4008. https://doi.org/10.1029/jb089ib06p03997

Passelègue, F. X., Spagnuolo, E., Violay, M., Nielsen, S., Di Toro, G., & Schubnel, A. (2016). Frictional evolution, acoustic emissions activity, and off-fault damage in simulated faults sheared at seismic slip rates: Off-fault damage due to thermal cracking. *Journal of Geophysical Research: Solid Earth*, *121*(10), 7490–7513. https://doi.org/10.1002/2016jb012988

Paul, P. K., Zoback, M. D., & Hennings, P. H. (2007). Fluid flow in a fractured reservoir using a geomechanically-constrained fault zone damage model for reservoir simulation. In *SPE annual technical conference and exhibition*.

Pec, M., & Al Nasser, S. (2021). Formation of nanocrystalline and amorphous materials causes parallel brittle-viscous flow of crustal rocks: Experiments on quartz-feldspar aggregates. *Journal of Geophysical Research: Solid Earth*, *126*(5), e2020JB021262. https://doi.org/10.1029/2020jb021262

Petley-Ragan, A., Ben-Zion, Y., Austrheim, H., Ildefonse, B., Renard, F., & Jamtveit, B. (2019). Dynamic earthquake rupture in the lower crust. *Science Advances*, *5*(7), 1–8. https://doi.org/10.1126/sciadv.aaw0913

Plimpton, S. (1995). Fast parallel algorithms for short—Range molecular dynamics. *Journal of Computational Physics*, *117*(1), 1–19. https://doi.org/10.1006/jcph.1995.1039

Prasher, C. L. (1987). *Crushing and grinding process handbook*. Wiley.

Ravi-Chandar, K., & Knauss, W. G. (1984). An experimental investigation into dynamic fracture: II. Microstructural aspects. *International Journal of Fracture*, *26*(1), 65–80. https://doi.org/10.1007/bf01152313

Reches, Z., & Dewers, T. A. (2005). Gouge formation by dynamic pulverization during earthquake rupture. *Earth and Planetary Science Letters*, *235*(1–2), 361–374. https://doi.org/10.1016/j.epsl.2005.04.009

Reches, Z., & Lockner, D. A. (1994). Nucleation and growth of faults in brittle rocks. *Journal of Geophysical Research*, *99*(B9), 18159–18173. https://doi.org/10.1029/94jb00115

Rempe, M., Mitchell, T., Renner, J., Nippress, S., Ben-Zion, Y., & Rockwell, T. (2013). Damage and seismic velocity structure of pulverized rocks near the San Andreas Fault. *Journal of Geophysical Research: Solid Earth*, *118*(6), 2813–2831. https://doi.org/10.1002/jgrb.50184

Rice, J. R., Sammis, C. G., & Parsons, R. (2005). Off-fault secondary failure induced by a dynamic slip pulse. *Bulletin of the Seismological Society of America*, *95*(1), 109–134. https://doi.org/10.1785/0120030166

Rudnicki, J. W. (1980). Fracture mechanics applied to the Earth's crust. *Annual Review of Earth and Planetary Sciences*, *8*(1), 489–525. https://doi.org/10.1146/annurev.ea.08.050180.002421

Sammis, C., King, G., & Biegel, R. (1987). The kinematics of gouge deformation. *Pure and Applied Geophysics*, *125*(5), 777–812. https://doi.org/10.1007/bf00878033

Sammis, C. G., & Ben-Zion, Y. (2008). Mechanics of grain-size reduction in fault zones. *Journal of Geophysical Research*, *113*(2), 1–12. https://doi.org/10.1029/2006jb004892

Sharon, E., & Fineberg, J. (1996). Microbranching instability and the dynamic fracture of brittle materials. *Physical Review B: Condensed Matter and Materials Physics*, *54*(10), 7128–7139. https://doi.org/10.1103/physrevb.54.7128

Sharon, E., & Fineberg, J. (1998). Universal features of the microbranching instability in dynamic fracture. *Philosophical Magazine B*, *78*(2), 243–251. https://doi.org/10.1080/014186398258302

Siman-Tov, S., Aharonov, E., Bonech, Y., & Rehes, Z. (2015). Fault mirrors along carbonate faults: Formation and destruction during shear experiments. *Earth and Planetary Science Letters*, *430*, 367–376. https://doi.org/10.1016/j.epsl.2015.08.031

Svetlizky, I., Kammer, D. S., Bayart, E., Cohen, G., & Fineberg, J. (2017). Brittle fracture theory predicts the equation of motion of frictional rupture fronts. *Physical Review Letters*, *118*(12), 125501. https://doi.org/10.1103/physrevlett.118.125501

Tapponnier, P., & Brace, W. F. (1976). Development of stress-induced microcracks in Westerly granite. *International Journal of Rock Mechancis and Mining Sciences*, *13*(4), 103–112. https://doi.org/10.1016/0148-9062(76)91937-9

Thomas, M. Y., & Bhat, H. S. (2018). Dynamic evolution of off-fault medium during an earthquake: A micromechanics based model. *Geophysical Journal International*, *214*(2), 1267–1280. https://doi.org/10.1093/gji/ggy129

Vashishta, P., Kalia, R. K., Rino, J. P., & Ebbsjö, I. (1990). Interaction potential for SiO_2: A molecular-dynamics study of structural correlations. *Physical Review B*, *41*(17), 12197–12209. https://doi.org/10.1103/physrevb.41.12197

Verberne, B. A., Plümper, O., Matthijs de Winter, D. A., & Spiers, C. J. (2014). Superplastic nanofibrous slip zones control seismogenic fault friction. *Science*, *346*(6215), 1342–1344. https://doi.org/10.1126/science.1259003

Vinh, P. C., & Ogden, R. W. (2005). On the Rayleigh wave speed in orthotropic elastic solids. *Meccanica*, *40*(2), 147–161. https://doi.org/10.1007/s11012-005-1603-6

Wilson, B., Dewers, T., Reches, Z., & Brune, J. (2005). Particle size and energetics of gouge from earthquake rupture zones. *Nature*, *434*(7034), 749–752. https://doi.org/10.1038/nature03433

Wilson, J. E., Chester, J. S., & Chester, F. M. (2003). Microfracture analysis of fault growth and wear processes, Punchbowl Fault, San Andreas system, California. *Journal of Structural Geology*, *25*(11), 1855–1873. https://doi.org/10.1016/s0191-8141(03)00036-1

Zhou, S. J., Lomdahl, P. S., Thomson, R., & Holian, B. L. (1996). Dynamic crack processes via molecular dynamics. *Physical Review Letters*, *76*(13), 2318–2321. https://doi.org/10.1103/physrevlett.76.2318